

Effect of Paint Baking Treatment on Mechanical Properties of Resistance Spot Welded Q&P 980 Steel

Dileep Chandran RAMACHANDRAN,^{1)*} Adib SALANDARI-RABORI,¹⁾ Abdelbaset R. H. MIDAWI,¹⁾ Andrew MACWAN²⁾ and Elliot BIRO¹⁾

1) Centre for Advanced Materials Joining, Department of Mechanical & Mechatronics Engineering, University of Waterloo, 200 University Avenue West, Waterloo, ON, N2L 3G1 Canada.

2) ArcelorMittal Global Research, 1390 Burlington Street East, Hamilton, ON, L8N 3J5 Canada.

(Received December 22, 2023; Accepted March 13, 2024; Advance online published March 22, 2024; Published May 15, 2024)

This study investigates the impact of paint baking on the macro and micro-mechanical properties of resistance spot welds in quenched and partitioned 980 steels. It is observed that paint baking enhances both peak load and energy absorption during cross-tension tests, as indicated by load-displacement curves. Four different regions were identified from the load-displacement curves after paint baking. An intriguing observation was a quick increase in the loading rate following a prior decrease, attributed to change in crack propagation behavior rather than improved work hardening. The study further simulated the upper-critical heat-affected zone using a Gleeble thermo-mechanical simulator to evaluate flow strength and work hardening. The Kocks-Mecking strain-hardening model was employed to analyze work hardening behavior in the studied conditions.

KEY WORDS: advanced high strength steels; work hardening; paint baking; crack; resistance spot welding.

1. Introduction

As a third-generation advanced high-strength steel (3G AHSS), quenched and partitioned (Q&P) steel is one of the materials being used to improve the crashworthiness and fuel economy of new-generation auto bodies.¹⁾ These properties rely on the specific combination of microstructures, based on the selectively designed alloying, and controlled thermo-mechanical processing.²⁾ However, reduction in post-welded tensile properties due to the softening at the subcritical heat-affected zone (SCHAZ), softening at the fusion boundary (FB), and liquation phenomenon after the resistance spot welding (RSW), have been reported as factors limiting wider use of 3G AHSSs.³⁾

To successfully implement 3G AHSS in automotive body parts, the cross-tension properties of these steels need to be improved significantly, as cross-tension strength (CTS) is a common proxy to estimate the crashworthiness properties of RSW.⁴⁾ In previous work⁵⁾ it was demonstrated that the softening along the FB, known as halo ring, can reduce the mechanical properties of the spot welds compared to the halo-free welds when tested in their as-welded state. During automotive manufacturing, the body-in-white structure

will be subjected to a paint-baking (PB) cycle to harden the paint. PB has been shown to modify weld microstructure and change the crack propagation path, improving the fracture properties of the RSW.⁶⁾ Based on a previous investigation into the impact of PB on the fracture behavior of Q&P 980 steel, it was observed that irrespective of the PB heat treatment, fracture propagation occurred within the upper critical heat-affected zone (UCHAZ). The fracture surface of the as-welded sample predominantly exhibited brittle intergranular fracture along the prior austenite grain boundaries (PAGBs). However, this brittle fracture mode was eliminated after PB treatment.⁷⁾

In general, during deformation, two main sources of dislocation generations exist: statistically stored dislocations (SSD), and geometrically necessary dislocations (GND).⁸⁾ The former is generated via Frank-Read sources, grain boundary ledges, *etc.*, during deformation and is the main source of dislocations generation during plastic deformation. GNDs are generated near interfaces (*e.g.*, grain boundaries, cell boundaries, *etc.*) due to a strain gradient.⁸⁾ Therefore, GNDs are produced to decrease strain mismatch and deformation inhomogeneity and do not contribute to the accommodation of plastic strain, as do SSDs.⁸⁻¹⁰⁾ Both SSDs and GNDs are known to contribute to the work hardening of metals with a more effective contribution from GNDs.⁸⁾

* Corresponding author: E-mail: dcramachandran@uwaterloo.ca



It was proposed that hardening from PB was due to static strain aging (SSA).¹¹⁾ This occurs via the SSA mechanism, which may influence the mechanical properties of steels via three different mechanisms, all occurring as a function of the PB temperature and time.^{12,13)} Firstly, there is the strain-induced ordering of solute atoms, explained by Snoek¹⁴⁾ and Wilson *et al.*¹⁵⁾ The second mechanism, Cottrell atmosphere, was introduced by Cottrell *et al.*,¹⁶⁾ occurs where strain aging is accompanied by dislocation pinning, which happens by interactions between interstitial atoms such as carbon and existing mobile dislocations. It should be also noted that a suitable amount of carbon should remain in the solid solution after PB (*e.g.*, decomposition of martensite, carbides, *etc.*) to produce a sufficient hardening effect during post-deformation.¹⁷⁾ Furthermore, Wilson *et al.*¹⁵⁾ proposed a third mechanism, where the formation of solute clusters eventually results in a fine transition carbide precipitation. In high-carbon martensitic steel, this transition carbide precipitation could be accompanied by the softening of the martensitic matrix,^{18,19)} which has been accepted as the precipitation of ϵ -carbides from PB improves cross-tension properties.²⁰⁾ The abovementioned theories regarding the strengthening effect of SSA have been explained and used to understand the hardening aspect of PB. Still, studies fall short of describing how PB can affect yield strengthening and work hardening and do not examine the underlying hardening micro-mechanisms.

Evaluating the local mechanical properties of weld zones is challenging due to their small size. To overcome the challenges associated with the small zones, various techniques have been used: thermo-mechanical simulation using Gleeble,^{21,22)} micro-tensile testing,²³⁾ hardness-scaling,²⁴⁾ mini-shear,²⁵⁾ and instrumented indentation.²⁶⁾ Considering the small scale and rounded nature of the investigated region, preparing mechanical specimens is impossible. Direct property measurement of the narrow HAZ is only possible using the instrumented indentation technique.

It is well known that the PB response of spot welds depends on a variety of features such as its as-welded microstructure, carbon content, dislocation density, and grain size. Thus, the PB response of low-carbon steel will be significantly different than a comparatively high-carbon Q&P 980 steel. Although the metallurgical aspects of PB

and its general hardening mechanisms are widely accepted, the micro- and macro-mechanical aspects of PB need further understanding. How PB alters the load-bearing capacity of the spot welds, work hardening behavior and the governing mechanisms have not been addressed systematically. Hence, this study, provides a detailed understanding of the changes in local mechanical properties of the upper critical heat affected zone (UCHAZ) of the Q&P 980 steel spot welds, before and after the paint baking treatment. Characterization of the local mechanical properties was done using micro-indentation test and tensile testing of Gleeble-simulated UCHAZ structures.

2. Materials and Methods

This study examines an industrially produced Zn-coated 1.2 mm thick Q&P 980 steel with a nominal chemical composition of 0.23 wt.% C, 2.01 wt.% Mn, 1.05 wt.% Si, and 0.22 wt.% Cr+Mo+Ti+Nb. The carbon equivalent of the material is 0.65 and was calculated according to the formula proposed by Yurioka *et al.*²⁷⁾ The microstructure of the as-received steel consists of a combination of ferrite (F), martensite (M), tempered martensite (TM), and retained austenite (RA), as shown in **Fig. 1**. Quantified microstructure of the base metal is reported elsewhere.⁵⁾

Resistance spot welding was carried out using a medium-frequency direct current (MFDC) robot with a C-type gun and a Rexroth Bosh weld controller. A dome-shaped Cu-Cr electrode with a flat face diameter of 6 mm was used for the welding. The welding schedules were chosen from AWS D8.9²⁸⁾ and are shown in **Table 1**. Optimization of these welding schedules and their effect on mechanical properties was already reported in previous work.^{5,29)}

To simulate the PB heat-treatment, the welded samples were heat-treated in a muffle furnace at a temperature of

Table 1. Welding schedule used in this study.

Electrode force (kN)	Welding schedule			Nugget diameter (mm)
	Squeeze time (ms)	Current (kA)	Welding time (ms)	
4	167	9.0	267	6.67

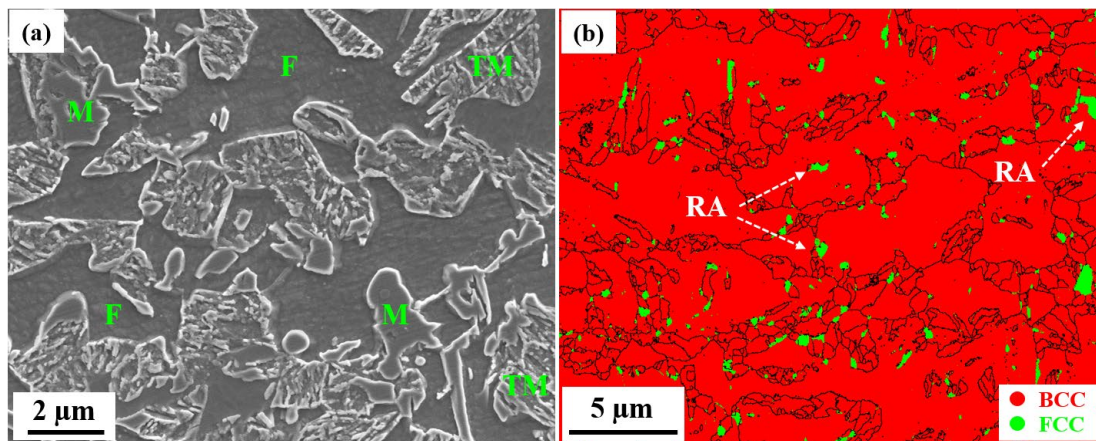


Fig. 1. (a) Base metal's SEM micrograph showing F, M, and TM, (b) electron backscatter diffraction phase map showing the RA. (Online version in color.)

180°C for 27 minutes. The parameters for PB were chosen through an extensive review of existing literature and consultations with automobile companies. The mechanical performance of the joints was evaluated by cross-tensile testing (CTT) according to AWS D8.9,²⁸⁾ using a crosshead speed of 10 mm/min on a 100 kN MTS frame. To measure the isolated tensile properties of the UCHAZ, the structure of the UCHAZ was simulated by thermo-mechanical simulation (Gleeble). The parameters used to create the UCHAZ structure are shown in Fig. 2. The heating rate and cooling rates are approximately 1 000°C/s, and 2 000°C/s, respectively. Furthermore, a holding time of 0.7 s was used in this study for Gleeble simulations. These parameters were evaluated using T-tests, a statistical analysis method employed to determine significant differences in data sets. To confirm the effectiveness of the heat treatment in replicating the microstructure and mechanical characteristics of the UCHAZ within the welded joint, the grain size and hardness of the Gleeble-simulated samples were evaluated and compared with those of the actual weld (AWS sample). PB treatments were also carried out on Gleeble simulated samples using the method described above. Tensile testing of the Gleeble samples was done using a Shimadzu universal tensile frame with a strain rate of 10⁻³ s⁻¹. Digital image correlation (DIC) apparatus (Vic 3D R9.1) was used to measure the strain during the tensile test.

Metallographic samples were prepared using standard methods. Samples were polished to a 1 μm diamond finish followed by etching with Bechet-Beaujard reagent.³⁾ The microstructure of the weld was characterized using an optical (Olympus BX51M) and a scanning electron microscopy (Zeiss UltraPlus FE-SEM) analysis. A JEOL JSM 7000F field emission SEM was used for the electron backscattered diffraction (EBSD) technique. To post-process the EBSD data, an Aztec crystal software was used.

Instrumented indentation testing was performed on a Nanovea-M1 indentation tester. To estimate the yield strength, a nearly flat tip indenter with a diameter of 50 μm was used by following the procedure suggested by Midawi *et al.*²⁵⁾ The yield strength of the weld before and after paint baking was calculated by Eq. (1) as suggested by Midawi

*et al.*²⁵⁾

$$\sigma_y = \frac{F_c}{2.2\pi a^2} \dots\dots\dots (1)$$

where σ_y is the yield strength, F_c is the force, and a is the radius of the indenter. Hereafter, samples welded according to the AWS schedule will be named, AWS, and AWS-PB for those that have undergone the PB treatment. Gleeble-simulated samples will be named G-AWS and G-AWS PB, respectively.

3. Results and Discussions

Optical micrographs (OM) of cross-sections from the AWS sample are shown in Fig. 3(a). Detailed base metal microstructure analysis and its quantified microstructure were given elsewhere.⁵⁾ Figures 3(b)–3(d) shows the microstructure of the UCHAZ, halo ring, and FB, respectively. The microstructure of the UCHAZ and fusion zone (FZ) is completely martensitic. The halo ring was 70–80 μm wide, and contained fewer sub-structures, as seen in Fig. 3(c). The detailed investigation of the halo ring microstructure may be found in previous work.⁵⁾ The FZ has a columnar dendritic structure due to the low G/R ratio, where the G and R are temperature gradient, and solidification rate, respectively. When CTT was done, it was seen that PB improved the load-bearing capacity of the spot welds by 34% and absorbed energy (area under the load-displacement curve up to the peak load) by 102%, as may be seen in Fig. 4(a).

PB increased the weld peak strength and energy absorption due to the cumulative effect of ε-carbide formation and the homogenization of microstructure after paint baking. The characterization of ε-carbide was documented in our prior research.⁷⁾ The ε-carbide has the ability to effectively pins the movement of dislocations and hinder the propagation of cracks. PB noticeably reduced elemental segregation and eliminated the solidified liquation formed after the welding.⁷⁾ Examination of the AWS-PB load-displacement curve shows that it may be divided into distinct regions. Region 1 displays a linear loading rate, Region 2 shows a gradual decrease in loading rate, followed by a sudden increase in loading rate (Region 3), and final fracture (Region 4). Of most interest, there is an increase in the slope of the load-displacement curve (Region 3) above a load of ~ 4.5 kN (Fig. 4(a)). To assess the loading behavior during the CTT, the derivative of the load (L) to its displacement (D) was plotted against the sample displacement in Fig. 4(b).

There are some similarities between the derivatives of the CTT curve and the Kocks-Mecking work hardening model³⁰⁾ (work hardening rate, *e.g.*, derivative of the true stress-strain curve, as a function of flow stress) in materials during Mode 1 loading (tensile stress normal to the plane of the crack), to show work hardening behavior.^{30,31)} Therefore, the derivatives of the load-displacement curve (Fig. 4(b)) are used to probe into the loading behavior of AWS and AWS-PB samples during CTT. The representative loading behavior is highlighted by the derivative of the load-displacement curve (filtered with a smoothing function to highlight the overall trend in the data) and matches with the identified regions from the load-displacement curve (Fig. 4(b)). The AWS sample solely exhibits the defined Region

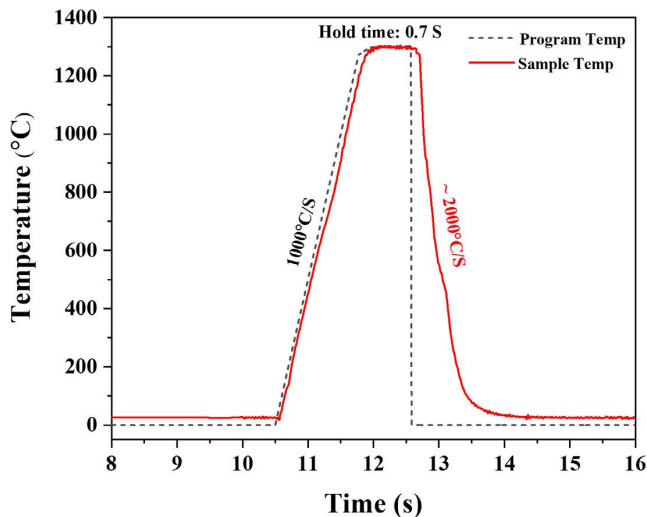


Fig. 2. Temperature profile of Gleeble simulations. (Online version in color.)

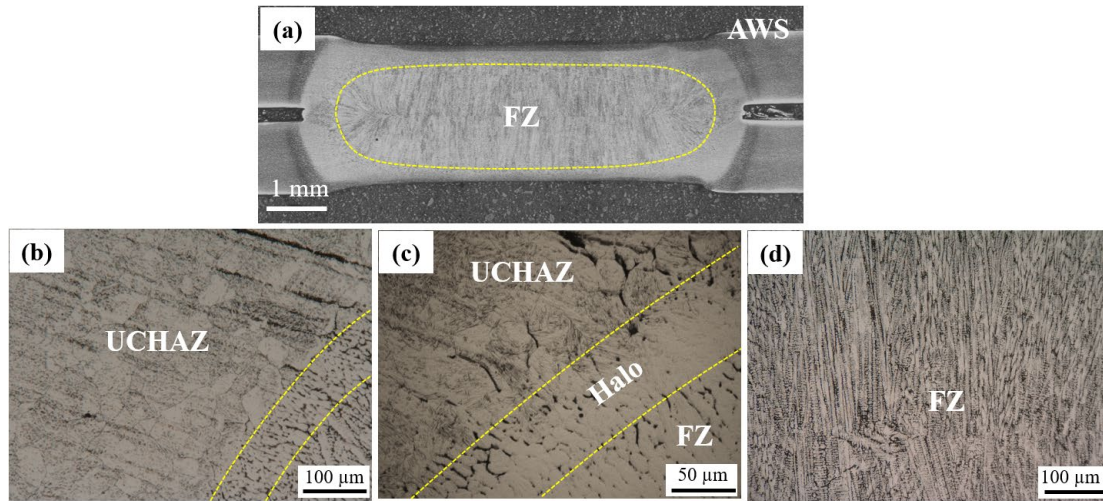


Fig. 3. Microstructure of the AWS sample: (a) cross-sectional micrograph, (b) UCHAZ, (c) halo ring, and (d) fusion zone. (Online version in color.)

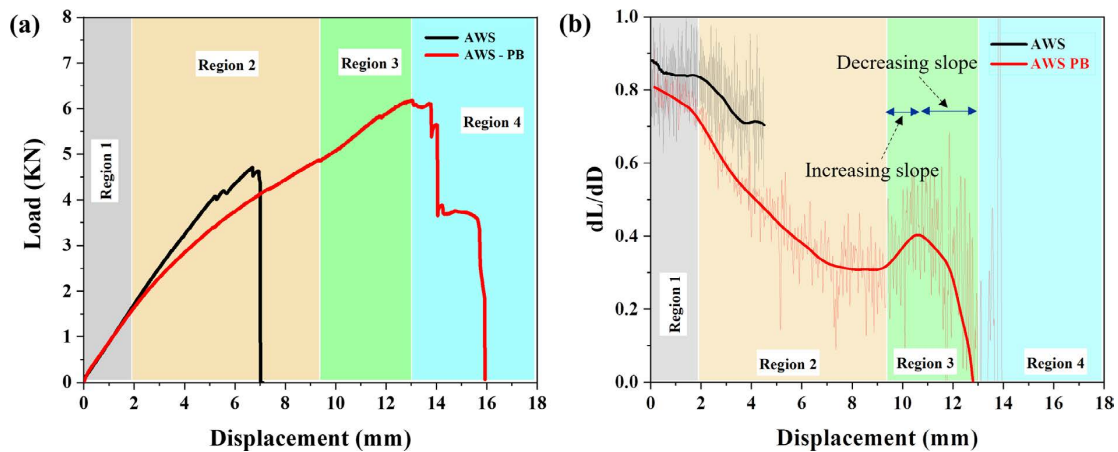


Fig. 4. Mechanical properties of the spot welds before and after paint baking: (a) CTT, (b) derivative of the load-displacement curve. (Online version in color.)

1 and 2, while the AWS-PB sample shows all four regions. It should be noted that the load-displacement behavior of the AWS-PB sample exhibits a strong resemblance to load-displacement curves documented in the literature.^{32,33} In Region 1, both the AWS and AWS-PB samples exhibit extensive bending of the base material, which is widely accepted in the literature.³⁰ In Region 2 (Fig. 4(a)), the two loading curves start deviating, implying the different loading behavior of the samples, resulting from the different microstructures. For both samples, starting in Region 2, the deformation localizes around the nugget (where the PB-AWS microstructure is different, from the AWS weld). At a displacement of 6 mm, the AWS sample fractures. Previous research demonstrates that the fracture surface of the AWS sample exhibits a brittle fracture behavior with an intergranular fracture path,⁷ aligning well with the load-displacement curve illustrated in Fig. 4(a).

The AWS-PB weld exhibits similar loading behavior to the AWS weld in Region 1, although the loading rate of the AWS-PB weld is slightly lower than exhibited by the AWS weld. However, the AWS-PB weld demonstrates distinct behavior in Regions 2 and 3 (Fig. 4(a)). As discussed, the differences in the microstructure surrounding the nugget in

the AWS-PB sample resulted in different loading behavior compared to the AWS weld. During testing of the AWS-PB sample, the load increases gradually in Region 2 and entering Region 3, a change in the slope of the load-displacement curve is seen (Fig. 4(a)). Despite a longer Region 2, Region 3 is shorter where the sample reaches the peak load, and fractures entering Region 4. As can be seen in Fig. 4(b), the loading rate decreased gradually in Region 2 until it reached a plateau by the end of this region. Entering Region 3, the loading rate (Fig. 4(b)) again initially increased, reached a maximum and then decreased. The reduction in loading rate continued until fracture in Region 4. To discuss this unique loading behavior, the microstructure of the AWS-PB needs to be investigated. For this purpose, an interrupted CTT was done, as shown in Fig. 5(a). SEM-EBSD is used to assess the microstructure of the interrupted sample (Figs. 5(b) and 5(c)).

It is important to emphasize that the interrupted sample (Fig. 5(a)) behaves in the same manner as the AWS-PB sample, further confirming the reproducibility of this load-displacement curve. A blended crack in the sheet-sheet interface can be seen in Fig. 5(b), which primarily confirms the strain localization around the nugget area in Region

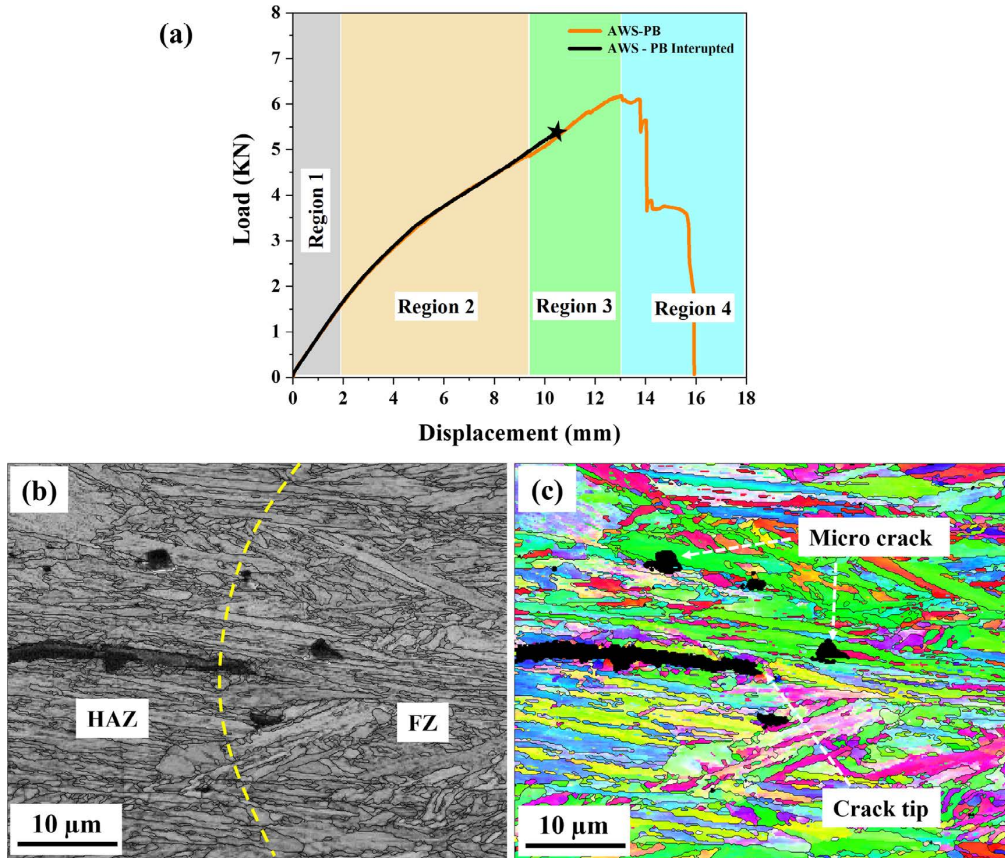


Fig. 5. (a) load-displacement curve with four regions shows the interrupted CTT, EBSD maps show the crack tip and the micro-cracks in the interrupted sample (b) IQ map and (c) IPF map. (Online version in color.)

3. The EBSD analysis also reveals the formation of small microcracks near the sheet-sheet interface, confirming that crack tip blunting occurred. By initiation of micro-cracks and blunting of the sheet-sheet interface cracks, the loading rate increases until the newly formed micro-cracks reach the critical propagation energy and start expanding through the microstructure, by which the loading rate will again decrease up to the fracture. Therefore, the improved energy absorption and fracture behavior of the AWS-PB sample can be attributed to this crack tip blunting and formation of micro-cracks, as they would have delayed crack propagation. Additionally, our prior research⁷⁾ indicates that PB resulted in decomposition of the martensite and the formation of ϵ -carbide, which increases fracture toughness by hindering dislocation movement. Moreover, PB alters the micro-texture, resulting in a more pronounced texture with most grains oriented $\langle 101 \rangle$ parallel to the rolling direction. This texture was reported to be better able to inhibit crack progress, raising the energy needed for crack propagation and changing the crack path, leading to a higher loading rate during CTT. This is well-discussed in our previous work.⁷⁾

Even by understanding crack propagation behavior in the AWS-PB weld, the connection between the increase in loading rate in Region 3 (Fig. 3(b)) and changes to the dislocation-obstacle interactions resulting from PB is unclear. To understand the changes in mechanical behavior, local mechanical properties needed to be assessed by focusing on the UCHAZ (Region 3) microstructure. For this purpose, the yield strength (YS) of the UCHAZ region was estimated for AWS and AWS-PB samples using instrumented indenta-

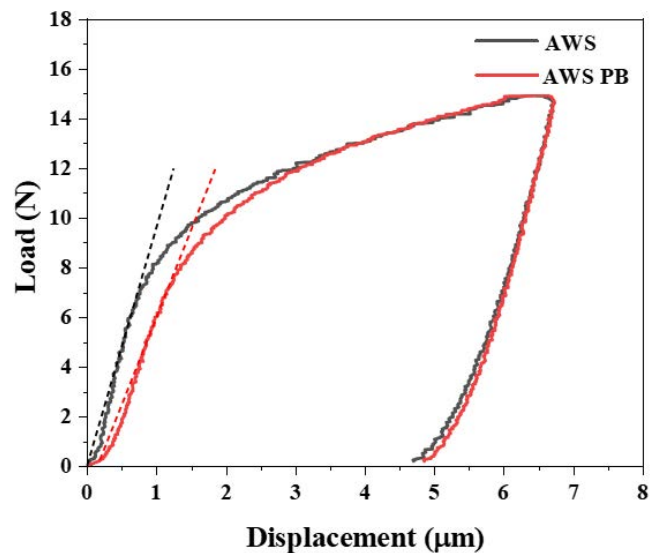


Fig. 6. Instrumented indentation load-displacement curves for Region 3 of AWS and AWS-PB samples. (Online version in color.)

tion.²⁵⁾ The load-displacement behavior shown in Fig. 6 for AWS and AWS-PB samples does not show any substantial changes, where there is only a slight difference in the YS. The YS of the AWS and AWS-PB samples are measured to be 1 248 and 1 189 MPa, respectively. The slight decrease in YS observed in AWS-PB sample can be attributed to the presence of softer microstructural features, such as decomposed martensite, in the UCHAZ. Therefore, it seems that

PB does not improve the local mechanical properties, *e.g.*, YS, contrary to the improvement seen in the macro-mechanical performance (cross-tension strength). To understand the effect of microstructural changes in UCHAZ (Region 3 microstructure) on local tensile properties, including the work hardening behavior, the UCHAZ was recreated using Gleeble and was mechanically tested.

The uniaxial tensile tests for Gleeble samples are presented in Fig. 7. The Gleeble samples are named G-AWS and G-AWS PB for before and after PB, respectively. The strain hardening rate ($d\sigma/d\varepsilon$) is determined by imposing the Kocks-Mecking model on the experimental data. The tensile sample geometry is shown in Fig. 7(a); a comprehensive explanation of the uniaxial tensile test procedure can be found elsewhere.⁷⁾

The true stress-strain curves (Fig. 7(b)) show the same broad behaviour of the cross-tension test (Fig. 4(a)), where the G-AWS exhibited brittle behavior, showing sudden fracture after yielding, and the G-AWS PB sample had supported large plastic deformation ($\sim 11\%$ elongation to fracture). However, due to the localization of the strain at the necked area, and the non-uniform plastic deformation behavior, only the data before necking (uniform plastic deformation region) was used to extract work hardening curves (Fig. 7(c)). For the identification of the necking strain, Considère criterion³⁴⁾ is used. The true stress at fracture and fracture strain was calculated using the cross-sectional area of the failed sample. As can be seen in Fig. 7(b), YS is 1 278 and 1 161 MPa for the G-AWS and G-AWS PB, respectively, which does not show a significant difference. These values align well with the yield strengths obtained from the actual welds (AWS and AWS-PB samples) by performing the micro-indentation (1 248 and 1 189 MPa, respectively). Hence, it can be assumed that the Gleeble-simulated samples well-represented the microstructure of specific weld regions.

From examining the work-hardening behavior of the samples, the G-AWS sample fractured immediately after yield-

ing, and only the elastic to plastic transition is observable with no distinct work-hardening stages (Fig. 7(c)). However, the G-AWS PB sample, exhibited Stage II (athermal hardening) and Stage III (dynamic recovery) work hardening after yielding. Stage II is typically accompanied by the persistent interaction of obstacles with dislocations and dislocation multiplications, where the work hardening rate shows a plateau (no further reduction in the work hardening rate).³⁵⁾ In Stage III, or dynamic recovery, dislocation substructures form a stage where dislocation density decreases due to the recovery processes, which is associated with a continuous reduction in the work hardening rate, until the fracture.³⁵⁾ However, these two stages are not distinguishable in the current data. Immediately after the elastic to plastic transition region, the work hardening rate continuously decreases until the start of necking. Compared to the CTT behaviour, it may be seen that the increase in loading rate in Region 3 (Fig. 4(b)) was not present in the work hardening curve of G-AWS PB. Therefore, it can be concluded that PB does not affect yield strengthening and work hardening behavior (micro-mechanical behavior). However, it does substantially improve the fracture and energy absorption behavior (macro-mechanical performance).⁷⁾ It is important to highlight that, increased elongation and work hardening of UCHAZ enables strain localization to be continued around the nugget before fracture, offering new areas of strain hardening, leading to the increase in loading rate in the CTS specimens.

The increase in loading rate seen in Region 3 of Fig. 4(b) is not solely attributed to the changes in the work hardening behaviour of the UCHAZ after PB. Another important factor that needs to be considered regarding the work-hardening behavior is the dislocation density. For post-deformation hardening to occur as a result of PB, both the amount of free carbon in the solid solution and the density of dislocation need to be above a critical limit. However, in most of the studies, the critical dislocation density required to activate the SSA mechanism is absent while those papers primarily

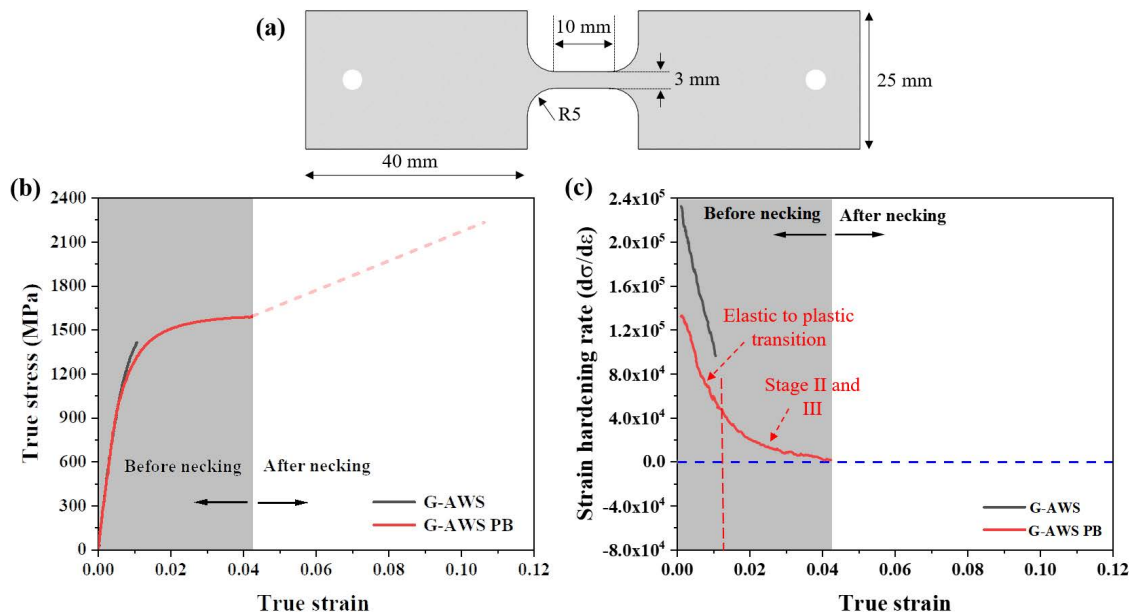


Fig. 7. (a) Gleeble simulated sample geometry for the tensile test, (b) true stress-strain behavior of the samples, and (c) derivative of the stress-strain curve showing the strain hardening behavior. (Online version in color.)

focus on the critical carbon content. It is also worth noting that PB leads to the redistribution of solute in the matrix and decreases elemental segregation, leading to a more homogenous microstructure.^{7,36} This implies that after PB there will be a low GND density as they are generated from microstructural inhomogeneities. Therefore, it is expected that GNDs will not have a significant influence on the SSD mechanism in the PB sample, although the carbon content in the solid solution may reach the critical limit. However, this needs a systematic study incorporating characterization techniques and interrupted tests to examine the evolution of dislocation density before and after PB as well as during tensile deformation, which is the topic of an ongoing study.

4. Conclusion

The present study examines the effect of paint baking on the macro and micro-mechanical behavior of resistance spot welded Q&P 980 steel. The results revealed that PB significantly enhanced the cross-tension strength (maximum weld strength) and energy absorption of the spot welds, with 34% in maximum weld strength and 102% in absorbed energy. Four distinct regions were identified for CTT load-displacement curves after the PB. It was found that Regions 2 and 3 involve the localization of deformation at the nugget area where in Region 3, the loading rate (derivative of load-displacement) surprisingly increased and then after reaching a maximum, decreased up to the fracture in Region 4. It was later shown that this unique loading behavior is due to the crack tip blunting and initiation of new micro-cracks. Uniaxial tensile behavior of the simulated microstructure of Region 3 (UCHAZ) did not show any significant difference in yield strengthening and work hardening behavior between the G-AWS and G-AWS PB samples. It was found that the G-AWS PB sample experienced Stage II and III work hardening, where these two stages were not distinguishable. However, the G-AWS sample only entered early Stage II right after elastic to plastic transition, before experiencing a premature fracture. Accordingly, it was concluded that the local mechanical performance of spot weld is not affected by paint baking, while the fracture and energy absorption behavior was improved substantially.

Acknowledgment

The authors would like to acknowledge the financial support from the Arcelor-Mittal Dofasco G.P. in Hamilton, Canada, and the Natural Sciences and Engineering Research Council (NSERC). The electron microscopy was performed at the Canadian Centre for Electron Microscopy (also supported by NSERC and other government agencies).

Disclosure Statement

The authors report there are no competing interests to declare.

REFERENCES

- M. Shojaee, A. R. H. Midawi, B. Barber, H. Ghassemi-Armaki, M. Worswick and E. Biro: *J. Manuf. Process.*, **65** (2021), 364. <https://doi.org/10.1016/J.JMAPRO.2021.03.047>
- G. Park, S. Uhm and C. Lee: *Mater. Sci. Eng. A*, **788** (2020), 139477. <https://doi.org/10.1016/J.MSEA.2020.139477>
- X. D. Liu, Y. B. Xu, R. D. K. Misra, F. Peng, Y. Wang and Y. B. Du: *J. Mater. Process. Technol.*, **263** (2019), 186. <https://doi.org/10.1016/j.jmatprotec.2018.08.018>
- M. Pouranvari and S. P. H. Marashi: *Sci. Technol. Weld. Join.*, **18** (2013), 361. <https://doi.org/10.1179/1362171813Y.0000000120>
- D. C. Ramachandran, B. Figueredo, O. Sherepenko, W. Jin, Y. Do Park and E. Biro: *J. Manuf. Process.*, **75** (2022), 320. <https://doi.org/10.1016/j.jmapro.2022.01.019>
- G. Park, K. Kim, S. Uhm and C. Lee: *Mater. Sci. Eng. A*, **766** (2019), 138401. <https://doi.org/10.1016/j.msea.2019.138401>
- D. C. Ramachandran, O. T. Betiku, M. Shojaee, A. Salandari-Rabori, A. R. H. Midawi, J. U. Kim, R. Bakhtiari, A. Macwan and E. Biro: *Mater. Charact.*, **206** (2023), 113383. <https://doi.org/10.1016/j.matchar.2023.113383>
- Z. Li, Z. Li, Z. Tan, D. B. Xiong and Q. Guo: *Int. J. Plast.*, **127** (2020), 102640. <https://doi.org/10.1016/J.IJPLAS.2019.12.003>
- D. A. Korzekwa, D. K. Matlock and G. Krauss: *Metall. Trans. A*, **15** (1984), 1221. <https://doi.org/10.1007/BF02644716>
- A. Salandari-Rabori, B. J. Diak and V. Fallah: *Mater. Sci. Eng. A*, **857** (2022), 144043. <https://doi.org/10.1016/j.msea.2022.144043>
- H. Järvinen, M. Honkanen, M. Järvenpää and P. Peura: *J. Mater. Process. Technol.*, **252** (2018), 90. <https://doi.org/10.1016/J.JMAT-PROTEC.2017.08.027>
- A. K. De, S. Vandeputte and B. C. De Cooman: *Scr. Mater.*, **41** (1999), 831. [https://doi.org/10.1016/S1359-6462\(99\)00232-8](https://doi.org/10.1016/S1359-6462(99)00232-8)
- T. Waterschoot, B. C. De Cooman, A. K. De and S. Vandeputte: *Metall. Mater. Trans. A* **2003** **343**, **34** (2003), 781. <https://doi.org/10.1007/S11661-003-0113-1>
- J. L. Snoek: *Physica*, **8** (1941), 711. [https://doi.org/10.1016/S0031-8914\(41\)90517-7](https://doi.org/10.1016/S0031-8914(41)90517-7)
- D. V. Wilson, B. Russell and J. D. Eshelby: *Acta Metall.*, **7** (1959), 628. [https://doi.org/10.1016/0001-6160\(59\)90132-4](https://doi.org/10.1016/0001-6160(59)90132-4)
- A. H. Cottrell and B. A. Bilby: *Proc. Phys. Soc. Sect. A*, **62** (1949), 49. <https://doi.org/10.1088/0370-1298/62/1/308>
- L. J. Baker, S. R. Daniel and J. D. Parker: *Mater. Sci. Technol.*, **18** (2002), 355. <https://doi.org/10.1179/026708302225002452>
- E. Biro, J. R. McDermid, S. Vignier and Y. Norman Zhou: *Mater. Sci. Eng. A*, **615** (2014), 395. <https://doi.org/10.1016/j.msea.2014.07.102>
- D. C. Ramachandran, A. R. H. Midawi, M. Shojaee, O. Sherepenko, H. Ghassemi-Armaki and E. Biro: *Materialia*, **26** (2022), 101644. <https://doi.org/10.1016/j.mtla.2022.101644>
- M. Jung, S.-J. Lee and Y.-K. Lee: *Metall. Mater. Trans. A* **2009** **403**, **40** (2009), 551. <https://doi.org/10.1007/S11661-008-9756-2>
- D. C. Saha, S. S. Nayak, E. Biro, A. P. Gerlich and Y. Zhou: *Metall. Mater. Trans. A Phys. Metall. Mater. Sci.*, **45** (2014), 6153. <https://doi.org/10.1007/s11661-014-2591-8>
- J. Wang, L. Yang, M. Sun, T. Liu and H. Li: *Mater. Des.*, **97** (2016), 118. <https://doi.org/10.1016/j.matdes.2016.02.071>
- Y. Ma, A. Takikawa, J. Nakanishi, K. Doira, T. Shimizu, Y. Lu and N. Ma: *Mater. Des.*, **201** (2021), 109505. <https://doi.org/10.1016/J.MATDES.2021.109505>
- A. Mohamadizadeh, E. Biro and M. Worswick: *Eng. Fract. Mech.*, **268** (2022), 108506. <https://doi.org/10.1016/j.engfracmech.2022.108506>
- A. R. H. Midawi, C. H. M. Simha and A. P. Gerlich: *Mater. Sci. Eng. A*, **675** (2016), 449. <https://doi.org/10.1016/J.MSEA.2016.08.056>
- S. Zhang, A. Ghatei-Kalashami, A. R. H. Midawi and N. Y. Zhou: *J. Manuf. Sci. Eng. Trans. ASME*, **144** (2022), 081006. <https://doi.org/10.1115/1.4053730>
- T. Kasuya and N. Yurioka: *Weld. Res. Suppl.*, **6** (1993), 263. https://app.aws.org/wj/supplement/WJ_1993_06_s263.pdf
- AWS: AWS D8.9M:2012 Test Methods for Evaluating the Resistance Spot Welding Behavior of Automotive Sheet Steel Materials, (1997), 1.
- B. Figueredo, D. C. Ramachandran, A. Macwan and E. Biro: *Weld. World*, **65** (2021), 2359. <https://doi.org/10.1007/s40194-021-01179-z>
- M. Bambach, I. Sizova, S. Bolz and S. Weiß: *Metals (Basel)*, **6** (2016), 204. <https://doi.org/10.3390/met6090204>
- Y. Z. Tian, L. J. Zhao, S. Chen, A. Shibata, Z. F. Zhang and N. Tsuji: *Sci. Rep.*, **5** (2015), 1. <https://doi.org/10.1038/srep16707>
- P. EftekhariMilani, E. M. van der Aa, R. Petrov, M. J. M. Hermans and I. M. Richardson: *Metall. Mater. Trans. A Phys. Metall. Mater. Sci.*, **49** (2018), 6185. <https://doi.org/10.1007/s11661-018-4912-9>
- M. Shamsujjoha, C. M. Enloe, A. C. Chuang, J. J. Coryell and H. Ghassemi-Armaki: *Materialia*, **15** (2021), 100975. <https://doi.org/10.1016/J.MTLA.2020.100975>
- I. S. Yasniov, A. Vinogradov and Y. Estrin: *Scr. Mater.*, **76** (2014), 37. <https://doi.org/10.1016/J.SCRIPTAMAT.2013.12.009>
- A. D. Rollett and U. F. Kocks: *Solid State Phenom.*, **35-36** (1993), 1. <https://doi.org/10.4028/www.scientific.net/ssp.35-36.1>
- S. M. Manladan, Y. J. Jang and Y. Do Park: *J. Mater. Res. Technol.*, **24** (2023), 4756. <https://doi.org/10.1016/j.jmrt.2023.04.144>